Modeling the temperature of the Litosphere through numerical studies of the Diffusion equation

Magnus S. Ingstad
(Dated: December 19, 2020)

We implemented the diffusion equation numerically to study how a subducting plate on the western coast of Norway 1 billion years ago might affect the temperature of the litosphere underneath Oslo today. Starting with discretizing the 1D diffusion equation, we implemented the Euler forward, Euler backward and Crank-Nicolson, and found that the latter gives more accurate results at high time-steps Δt. At lower Δt, we found that the Euler methods were comparable, especially for equilibrium states that are close to linear. Proceeding with the forward Euler method, we extended to the 2D diffusion equation and determined a suitable choice of $\Delta x = 0.01$ and $\Delta t < 0.025\Delta x^2$ for a non-dimensional system with $u(x,t), x \in [0,1]$. Scaling the litosphere model, we used these choice of parameters and found that the proposed subduction plate should lead to about 5% temperature increase in the crust and 10% temperature increase in the lower mantle compared to the situation without this plate.

I. INTRODUCTION

Partial differential equations generally represent the change in some quantity with some set of variables, e.g. time and space. As such, these can be broadly applied to describe physical systems, which in turn can be used to model the inner workings of the world around us. One such physical system is the litosphere which starts right under our feet and stretches about 100 km into the earth. Through some simplifications, we want to use the diffusion equation to study how a proposed subduction zone on the western coast of Norway about 1 billion years ago can have effect on the temperature in the crust and the mantle today.

We start by presenting the diffusion equation in one dimension with respect to some general quantity $u(x,t)$, discretize it, and look at three different schemes for advancing it forward in time. Choosing one, we move on to a general two dimensional system with $u(x,y,t)$, and study how the step length in space and time must be selected for a stable and accurate solution by comparing to analytical results. We then move on to the physical case of the litosphere by representing it as such a 2D system, and making the diffusion equation dimensionless to bring it over the general form we already looked at. We then consider some different ways of modeling the heat production in the litosphere and estimate what change of temperature the proposed subducted slab may have caused.

II. METHOD

The diffusion equation can be formulated in the multi-dimensional case as

$$\nabla^2 \mathbf{u}(\mathbf{x}, t) = \frac{\partial \mathbf{u}(\mathbf{x}, t)}{\partial t}, \tag{1}$$

where we have second order derivatives of space contained in ∇ on the left hand side and the partial time derivative ∂t on the right hand side. These are applied to some function $\mathbf{u}(x,t)$, which is what we want to solve.

A. One dimensional case

To investigate some different algorithms for solving the problem numerically, we first consider the one dimensional case where x is the only space-dependent variable, making the equation a PDE in two dimensions, given by

$$\frac{\partial^2 u(x,t)}{\partial x^2} = \frac{\partial u(x,t)}{\partial t}, \quad t > 0, \quad x \in [0,L]. \tag{2}$$

For this report, we will use the convenient notation $u_{xx} = u_t$ to represent this equation. Aiming for a non-dimensional analysis we let $L = 1$ and consider boundary conditions

$$u(0,t) = 0 \quad t \geq 0, \qquad u(L,t) = 1 \quad t \geq 0.$$

For the initial conditions at $t = 0$, we let u be zero everywhere but at the boundaries, i.e.

$$u(x,0) = 0, \quad 0 < x < L$$

For the numerical approximation, we first discretize the continuous differential equation by $n+2$ evenly spread points for $0 \leq x \leq 1$, resulting in a step length of $\delta x = 1/(n + 1)$ between each point. The n points between the boundaries are what we need to update with time, for which we need a discrete timestep Δt. With this discretization, we will implement three different algorithms for advancing a solution at a time-step k u_i^k forward in time to obtain $u_i^{(k+1)}$. These are the explicit Euler Forward, the implicit Euler Backward, and the Crank-Nicolson methods.

To advance the solution in time, we start by considering the differential equation (2), where we need numerical

expressions for both the time derivative u_t and the double spatial derivative $u_x x$.

For the former, we have by the first order Taylor expansion of $u(x,t)$ with respect to t at $t \pm \Delta t$

$$u(x,t) = u(x, t \pm \Delta t) + \frac{\partial}{\partial t}u(x,t)(\pm \Delta t) + \mathcal{O}((\Delta t)^2)$$

$$\implies u_t = \frac{\partial}{\partial t}u(x,t) = \frac{u(x, t \pm \Delta t) - u(x,t)}{\pm \Delta t} + \mathcal{O}(\Delta t).$$

This approximation has a first order local truncation error Δt. Choosing a positive sign for $+\Delta t$ results in the forward Euler scheme, where $t + \Delta t$ represents the time-advanced state. On the other hand, a negative sign for $-\Delta t$ results in the backward Euler scheme, where t represents the time-advanced state and $t - \Delta t$ the previous state.

For the spatial derivative u_{xx} we will use the second order central finite difference, which by [1] is given by

$$u_{xx} = \frac{u(x + \Delta x, t) - 2u(x,t) + u(x - \Delta x, t)}{\Delta x^2} + \mathcal{O}((\Delta x)^2),$$

where we have a second order local truncation error $(\Delta x)^2$. Inserting into (2) along with u_t we first find for the Forward Euler scheme

$$\frac{u_{i+1}^k - 2u_i^k + u_{i-1}^k}{\Delta x^2} + \mathcal{O}(\Delta x^2) = \frac{u_i^{k+1} - u_i^k}{\Delta t} + \mathcal{O}(\Delta t).$$

Here, we note that the time advanced solution $u_i^{(k+1)}$ only appears once in this equation such that we can find an explicit expression for this quantity, hence Forward Euler is an explicit method. In particular, we define $\alpha = \Delta t / \Delta x$ and solve for $u_i^{(k+1)}$ to get the expression

$$u_i^{k+1} = \alpha(u_{i+1}^k + u_{i-1}^k) + (1 - 2\alpha)u_i^k, \qquad (3)$$

which gives the necessary algorithm to solve this case numerically. For the Backward Euler scheme, we insert the same expression for u_{xx} and the alternate expression for u_t into (2) to get

$$\frac{u_{i+1}^k - 2u_i^k + u_{i-1}^k}{\Delta x^2} + \mathcal{O}(\Delta x^2) = \frac{u_i^k - u_i^{k-1}}{\Delta t} + \mathcal{O}(\Delta t),$$

where the previous timestep u_i^{k-1} is now the separated value. Defining α as before, solving for this gives

$$u_i^{k-1} = -\alpha(u_{i+1}^k + u_{i-1}^k) + (1 - 2\alpha)u_i^k. \qquad (4)$$

While the explicit scheme could be represented as $u_i^{k+1} = \hat{A}u_{i-1,i,i+1}^k$ for some operator $\hat{A}$, we now have the case $u_i^{k-1} = \hat{A}u_{i-1,i,i+1}^k$ where the time advanced solution is behind the operator. In fact, this operator can be represented by the matrix

$$\hat{A} = \begin{bmatrix} 1+2\alpha & -\alpha & 0 & \dots & & 0 \\ -\alpha & 1+2\alpha & -\alpha & 0 & & \vdots \\ 0 & \ddots & \ddots & \ddots & & 0 \\ \vdots & \ddots & \ddots & \ddots & & -\alpha \\ 0 & \dots & 0 & -\alpha & 1+2\alpha \end{bmatrix},$$

where we have

$$\hat{u}^{k-1} = \begin{bmatrix} u_0^{k-1} \\ u_1^{k-1} \\ \vdots \\ u_{n+1}^{k-1} \end{bmatrix}, \quad \hat{u}^k = \begin{bmatrix} u_0^k \\ u_1^k \\ \vdots \\ u_{n+1}^k \end{bmatrix}.$$

Note that since the boundaries contain no neighbours, the upper and lower rows of the matrix do not represent the full solution in (4). Since we have boundaries of $u_0^k = 0$ and $u_{n+1}^k = 1$ for all values of k, the full solution here is just $u_0^k = u_0^{k-1}$ and $u_{n+1}^k = u_{n+1}^{k-1}$. This can be achieved by simply letting the first element of the top row be equal to 1 while all other elements are equal to 0, while similarly only having a value for the last element at 1 for the bottom row.

Doing this, we now have the differential equation with its boundaries represented as a matrix equation by the backward Euler method. This can be solved by inverting the matrix $\hat{A}$ and multiplying it on both sides of the equation, giving $\hat{u}^k = \hat{A}^{-1}\hat{u}^{k-1}$. Instead of performing the inversion explicitly however, we note that as a tridiagonal matrix, this problem can be solved more cheaply by Gauss eliminations at a computational complexity of $\mathcal{O}(n)$. We use the implementation of this from earlier work.

The final algorithm we will consider is the Crank-Nicolson scheme [2]. From [1], we have that this scheme can be represented by the equation

$$-\alpha(u_{i+1}^k + u_{i-1}^k) + (2 + 2\alpha)u_i^k$$
$$= \alpha(u_{i+1}^{k-1} + u_{i-1}^{k-1}) + (2 - 2\alpha)u_i^{k-1}.$$

Like the backward Euler scheme, this can expressed as a matrix equation. If we let the matrix $\hat{B}$ be given by

$$\hat{B} = \begin{bmatrix} 2 & -1 & 0 & \dots \\ -1 & 2 & -1 & 0 \\ 0 & \ddots & \ddots & -1 \\ \vdots & \ddots & -1 & 2 \end{bmatrix},$$

and $\hat{B}_1 = (2\hat{I} + \alpha\hat{B})$, $\hat{B}_2 = (2\hat{I} - \alpha\hat{B})$ where $\hat{I}$ is the identity matrix, then the equation becomes

$$\hat{B}_1\hat{u}^k = \hat{B}_2\hat{u}^{k-1}.$$

To ensure the correct boundary conditions we redefine the bottom and top rows of $\hat{B}_1$ and $\hat{B}_2$ as we did for

$\hat{B}$. Implementing the Crank-Nicolson scheme can then be done by first calculating $\hat{u}' = \hat{B}_2\hat{u}^{k-1}$, then solving the system $\hat{B}_1\hat{u}^k = \hat{u}'$ with the same tridiagonal matrix solver as for the backward euler scheme.

Note that by [1], we have that the local truncation error of the Crank-Nicolson method is of order Δx^2 in space and Δt^2 in time. This is the same error we found for the Euler methods with respect to space, but one order lower with respect to time, making the method more accurate for similar timesteps.

Another important thing to consider when evaluating these methods is their stability. Although both the Euler methods have the same local truncation error, we know from [1] that for the explicit forward Euler scheme, choosing α such that the expression $(1-2\alpha)$ in front of u_i^k in (3) would result in instabilities. This corresponds to a choice of $\alpha > 0.5$. For the backward Euler and Crank-Nicolson schemes, this is not the case as these are implicit methods, and we thus have that these methods are stable for any choice of α. Unlike the forward Euler method where only certain choice of $\alpha = \delta t / \delta x^2 < 0.5$ is stable.

To further evaluate these properties, the choice of conditions for (2) leads to an analytical solution for $u(x,t)$ which we will use as a benchmark for the different methods. This solution is found in VI to be given by (8), where

$$u(x,t) = x + \sum_{n=1}^{\infty} \frac{2 \cdot (-1)^n}{\pi n} sin(n\pi x) e^{-(n\pi)^2 t}.$$

Implementing this numerically, we sum over n until the a new term changes the solution by less than a tolerance of 10^{-8}. This is done separately for each discrete point in x. We then compare the analytical solution to the numerical solutions at two different times $t_1 = 0.1$ and $t_2 = 0.3$, representing two different states of $u(x,t)$.

B. Two-dimensional case

To further consider a two-dimensional case, we now use an additional dimension y in space such that (1) reduces to

$$\frac{\partial^2 u(x,y,t)}{\partial x^2} + \frac{\partial^2 u(x,y,t)}{\partial y^2} = \frac{\partial u(x,y,t)}{\partial t}, t > 0, x, y \in [0,1],$$

using the same value of $L = 1$, now in both spatial dimensions. This is then essentially a box of size 1×1. Alternatively expressed in terms of the short-hand notation we have $u_{xx} + u_{yy} = u_t$. For the discretization, we choose $nx+2$ evenly spread points in the x-direction, and $ny + 2$ evenly spread points in the y-direction.

To solve this numerically, we proceed as before by taking the central difference approximation of the second order derivatives

$$u_{xx}^{ij} = \frac{u_{(i-1),j} + u_{(i+1),j} - 2u_{i,j}}{(\Delta x)^2}$$

$$u_{yy}^{ij} = \frac{u_{i,(j-1)} + u_{i,(j+1)} - 2u_{i,j}}{(\Delta y)^2}$$

Choosing $\Delta x = \Delta y$ we further get for the left hand side

$$\frac{u_{(i-1),j} + u_{(i+1),j} + u_{i,(j-1)} + u_{i,(j+1)} - 4u_{i,j}}{(\Delta x)^2}.$$

Using the Forward Euler explicit scheme, the right hand side becomes the same as found before, so solving with respect to the time advanced solution we get

$$u_{i,j}^{k+1} = u_{i,j}^k(1-4\alpha) + \alpha(u_{(i-1),j}^k + u_{(i+1),j}^k + u_{i,(j-1)}^k + u_{i,(j+1)}^k), \tag{5}$$

having defined $\alpha = \frac{\Delta t}{(\Delta x)^2}$ as before. Note that we now get a stricter stability condition of $\alpha < 1/4$ because of $(1 - 4\alpha)$.

For the initial conditions, we extend those from before with

$$u(x,y,t=0) = 0, \quad 0 < x < L, \quad 0 < y < L.$$

As for the boundary conditions, these are no longer points but rather 4 1D boundaries at x, y equal to 0 and L. We first consider periodic boundary conditions in x, while in y we impose the similar boundaries as the 1D case where $u(x, y = 0, t) = 0$ and $u(x, y = L, t) = 1$. With the symmetric initial conditions, we would then get $\partial u/\partial x^2 = 0$ always, and the problem reduces to the 1D case. Each column x_i should then have the same analytical solution (8) as the 1D case, which we will use to evaluate the stability and accuracy of the algorithm as it varies with choice of Δx and Δt.

For a more interesting result which cannot be represented by a 1D solution, we also consider boundaries of

$$u(0,y,t) = 0 \quad t \geq 0, \quad u(L,y,t) = 1 \quad t \geq 0,$$

and

$$u(x,0,t) = 0 \quad t \geq 0, \quad u(x,L,t) = 1 \quad t \geq 0.$$

This should yield a situation where the right and top edges of the box are always equal to 1, while the left and bottom edges are always equal to 0.

C. Litosphere temperature distribution

Moving onto modeling the litosphere, we have that the governing equation is given by

$$\vec{\nabla}(k\vec{\nabla}T) + Q = \rho c_p \frac{\partial T}{\partial t} \tag{6}$$

where T is the temperature, ρ is the density, k is the thermal conductivity, c_p is the specific heat capacity and Q is the heat production. Here, we assume a constant density for the lithosphere of $\rho = 3.5 \cdot 10^3 \, kg/m^3$, a constant thermal conductivity of $k = 2.5 \, W/m/^{\circ}C$ and a

constant specific heat capacity of $c_p = 1000\,J/kg/^\circ C$. This assumption of constant values means that we can move k outside the first gradient on the left hand side, and that we can further scale the equation in terms of dimensionless quantities. Doing this will allow us to use the methods developed previously, although slightly modified because of the added term Q which represents additional heat from radioactive enrichment.

To gather the constants, we first divide by k on both sides of the equation. Note that the heat capacity Q has units of W/m^3, so divided by k we get $^\circ C/m^2$ which is consistent with $\nabla^2 T$ as it should. To make these quantities dimensionless we then need to multiply by some with units of $m^2/^\circ C$. To ensure similarity to the mathematical 2D model, we do this by writing

$$\hat{\nabla} = 120\,\text{km}\nabla, \quad \hat{T} = \frac{T}{1300^\circ C},$$

$$\hat{Q} = \frac{(120\,\text{km})^2}{1300^\circ C}\frac{Q}{2.5\,W/m/^\circ C} = \frac{1.2^2 \cdot 10^{10}}{1.3 \cdot 10^3 \cdot 2.5}\frac{m^3}{W}Q$$

$$\approx 4.431 \cdot 10^6 \frac{m^3}{W}Q = 4.431\frac{m^3}{\mu W}.$$

With these multiplications, the right hand side of (6) now reads $120^2 \rho c_p/k \frac{\partial \hat{T}}{\partial t}\,\text{km}^2$. For similarity, we want to introduce $\hat{t}$ such that it instead becomes $\partial \hat{T}/\partial \hat{t}$. We see that this requires

$$\hat{t} = \frac{k}{\rho c_p}\frac{1}{120^2\,\text{km}^2}t = \frac{2.5\,W/m/^\circ C}{3.5 \cdot 10^3\,kg/m^3 1000\,J/kg/^\circ C 120^2\,\text{km}^2}t$$

$$= \frac{2.5}{3.5 \cdot 10^3 \cdot 10^3 \cdot 1.2^2 \cdot 10^{10}} \cdot \frac{J/s/m/^\circ C}{kg/m^3 J/kg/^\circ C m^2}t$$

$$= \frac{2.5}{1.44 \cdot 3.5} \cdot 10^{-16}\,t/s \approx 1.877 \cdot 10^{-11}\,t/\text{yr} = 0.01877\,t/\text{Gyr}$$

With these dimensionless quantities, (6) now reads

$$\hat{\nabla}^2\hat{T} + \hat{Q} = \frac{\partial \hat{T}}{\partial \hat{t}} \iff T_{xx} + T_{yy} + Q = T_t, \quad (7)$$

where we have excluded the hats to simplify the notation in the last expression. Following the approach from before we would get a similar equation as in (5), now with $\alpha = \Delta\hat{t}/(\Delta\hat{x})^2$. We would also get an extra factor of $\hat{Q}\Delta\hat{t}$ on the right hand side of the expression in (5). When solving for $T_{i,j}^{(k+1)}$, Q would then be evaluated at $Q_{i,j}^k$. Variations in this value is what we want to study for the end of this report to see how the subduction plate might have affected the litosphere.

In particular, we separate the lithosphere into three parts, where the upper crust ranges from 0 to 20 km depth, the lower crust from 20 to 40 km depth, while the mantle ranges from 40 to 120 km depth. In these parts, the heat production is set to respectively 1.4, 0.35 and 0.05 $\mu W/m^3$ without considering the plate. Multiplying the numerical values by 4.431, we get the corresponding values in terms of $\hat{Q}$ to be used in our equations.

We first consider the case of no additional radiation from the plate, so that this is the only source of heat. Then we add an extra contribution of $0.5\,\mu W/m^3$ to the mantle to represent additional contribution from the plate. This contribution happens in a width of 150 km in values of x, or $150km/120km = 1.25$ in terms of $\hat{x}$. Finally, we consider a situation of radiactive decay, where the extra contribution decays, following 40% U, 20% Th and 20% K. These elements have half lives of respectively 4.47, 14.0 and 1.25 Gyr. In terms of reduced time $\hat{t}$, these values become respectively 0.08391, 0.26280 and 0.02346.

We start by simulating forward in time a state without any radiation, including the standard heat production all across the litosphere. After reaching an equilibrium state, we then implement the three cases mentioned above, which we label case 1, case 2 and case 3 respectively. We advance these forward $1Gyr$ in real time, equivalent to 0.01877 in dimensionless time. We also include results of case 2 and 3 where we have advanced forward a total of $20Gyr$.

III. RESULTS

A. 1D case

Plotted in figure 1 are the analytical and computed solutions at the two times $t_1 = 0.1$ and $t_2 = 0.3$. From the figure we see that the chosen points in time correspond to a curved $u(x,t_1)$ and an almost linear $u(x,t_2)$. We also see that the computed solutions from all the three algorithms overlap almost entirely with the analytical solution. We therefore did not include a similar plot for $\Delta x = 0.01$, as it would give even better numerical approximations and no new information.

Instead, we investigated the difference between the analytical and numerical solutions as a function of x $\epsilon(x)$. This is shown in figure 2 with results for the two different times t_1 and t_2. Here, we see that overall the Crank-Nicolson scheme lies closer to $\epsilon = 0$ for both the near-linear and curved solutions. The Euler forward and Euler backward scheme have a difference of opposite sign to the analytical solution, but are both at similar distances.

Note that the error here is the accumulated error from $t = 0$ to $t = t_i$, i.e. the Global error. To further investigate the properties of this error, we calculated its mean absolute value over the range of x-values, and studied its dependence on Δt in figures 3 and 4 at t_1 and t_2 respectively. These plots include results evaluated at both $\Delta x = 0.1$ and $\Delta x = 0.01$, where the $\Delta t = m\Delta x^2$ values are defined by 17 multipliers m in the range $[2^{-6}, 2^{2.5}]$.

From the first plot 3 at $t_1 = 0.1$ we see that at low Δt, all the numerical schemes give similar errors that are approximately 100 times higher at $\Delta x = 0.1$ than at $\Delta x = 0.01$. Towards higher Δt the error in the EF (Euler forward) and EB (Euler backward) schemes start
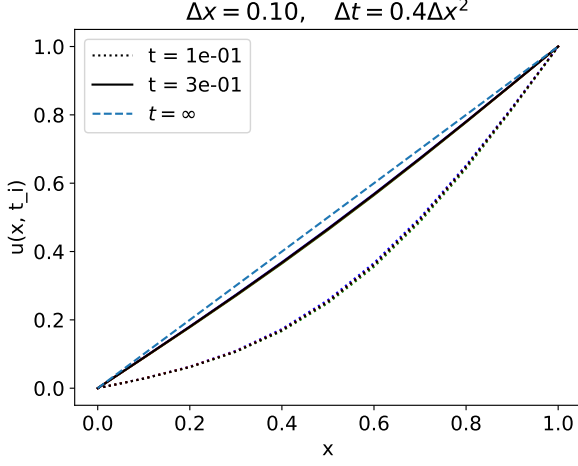
Figure 1. System solved with $\Delta x = 0.1$ and $\Delta t = 0.4\Delta x^2 = 0.004$. Plotted in dashed blue is the line x which corresponds to the solution at $u(x, t = \infty)$. The solutions at $t = 0.1$ are plotted as dotted lines, and at $t = 0.3$ as solid lines. The plot contains the analytical solution, the euler forward solution, the euler backward solution and the Crank-Nicolson solution in black, blue, green and red respectively.
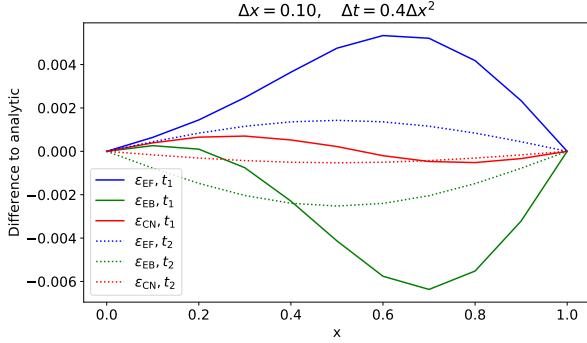

Figure 2. Difference $u(x, t_i) - f(x, t_i)$ where f is the exact solution. u is evaluated using the three numerical schemes Euler forward, Euler Backward and Crank-Nicolson, plotted in blue, green and red respectively. The difference is evaluated at $t_1 = 0.1$ and $t_2 = 0.3$ plotted with solid and dotted lines respectively. Used parameters $\Delta x = 0.1$ and $\Delta t = 0.4\Delta x^2$.

to increase in parallel to the line $\propto \Delta t$. At $m = 0.5$, the EF error increases a lot, going outside the limits of the plot for $\Delta x = 0.01$, while the EB error continues to increase with linearly with Δt. The CN (Crank-Nicolson) error maintains the same error for m up to ≈ 1 when it starts to increase faster than the Euler methods at $\Delta x = 0.1$. At $\Delta x = 0.01$ it remains near the same error for all Δt.
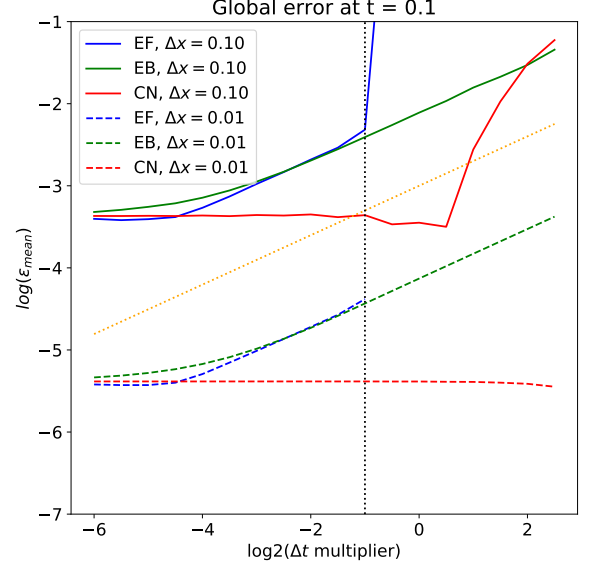

Figure 3. Mean absolute value of the accumulated error along the y-axis at $t = 0.1$. Plotted in blue, green and red are the EF, EB and CN schemes respectively. The dashed lines correspond to $\Delta x = 0.01$ and the solid lines $\Delta x = 0.1$. Along the x-axis is $log_2 m$ where $\Delta t = m\Delta x^2$. Plotted as an orange dotted line is a reference linear growth with $\propto \Delta t$, and plotted as a vertical black dotted line is $m = 0.5$, at the expected stability limit for EF.
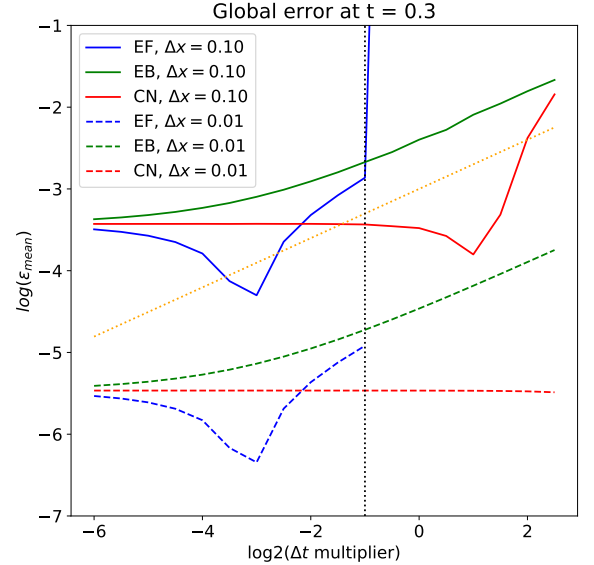

Figure 4. Same parameters as figure 3, except at $t = 0.3$ where $u(x, t)$ is almost linear.

From the second plot 4 at $t_2 = 0.3$, we see that both the implicit algorithms follow similar behavior and errors as

for $t_1 = 0.1$. The implicit EF however initially decreases in error with Δt before it starts to increase as before and becomes unstable at $m = 0.5$. This results in the EF method giving the least error for a wide range of Δt in this case. Note that t_1 and t_2 are when the numerical schemes approximate the curves shown in figure 1.

B. 2D case

Moving on to the 2D equation with spatial variables x and y, the error analysis with periodic boundaries along one axis gave the results shown in table I and II. These tables show the mean absolute difference between the analytical and numerical solutions. The former corresponding to the accumulated difference from $t = 0$ to $t = 0.2$, and the latter one timestep forward from $t = 0.2$. These are then the global and local errors respectively

From the global error in table I, we see that doubling Δx results in an approximate doubling of the error. We further see that changing Δt gives no change in error, except for $m = 0.4 > 0.25$ larger than the found stability limit where the error goes to ∞ as $\Delta x \to 0$. In total, we then get a global error $\epsilon_{\text{global}} \propto \Delta x$.

From the local error in table II we first note that the errors are lower for the same combination of Δx and Δt for the global error. Further, we see that doubling Δx again results in an approximate doubling of the error, while doubling Δt now gives a doubling of the error. The results beyond the stability limit at $m = 0.4$ are no longer unstable in comparison. In total, we get a local error of $\epsilon_{\text{local}} \propto \Delta x \Delta t$.

Table I. **Global error.** Mean absolute difference between analytical solution and numerical result after $t = 0.2$. First column shows chosen m for $\Delta t = m\Delta x^2$ and first row shows chosen Δx.

Δt multiplier $\backslash \Delta x$	0.025	0.05	0.1	0.2
0.1	4.88e-02	9.52e-02	1.82e-01	3.33e-01
0.2	4.88e-02	9.52e-02	1.82e-01	3.33e-01
0.4	∞	∞	1.79e78	2.36e04

Table II. **Local error.** Mean absolute difference between analytical solution and numerical after advancing one time-step from $t = 0.2$. First column shows chosen m for $\Delta t = m\Delta x^2$ and first row shows chosen Δx.

Δt multiplier $\backslash \Delta x$	0.025	0.05	0.1	0.2
0.1	2.56e-03	5.26e-03	1.11e-02	2.50e-02
0.2	5.13e-03	1.05e-02	2.22e-02	5.00e-02
0.4	1.03e-02	2.11e-02	4.45e-02	1.00e-01

Choosing Δx sufficiently low and Δt within the stability limit should then yield satisfying accuracy for further analysis. To check that the results seem reasonable for
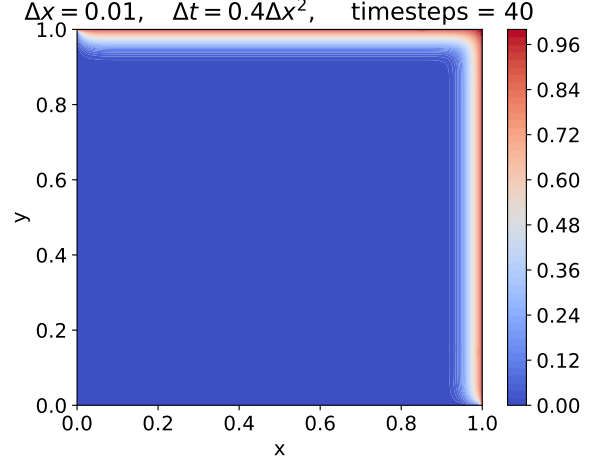

Figure 5. $u(x, y, t)$ solved with (5) with $\Delta x = \Delta y = 0.01$ and $\Delta t = 0.4\Delta x^2 = 0.4 \cdot 10^{-4}$ for 40 time-steps. Blue color points more towards the initial conditions of $u = 0$ and red towards the upper and left boundaries at $u = 1$.
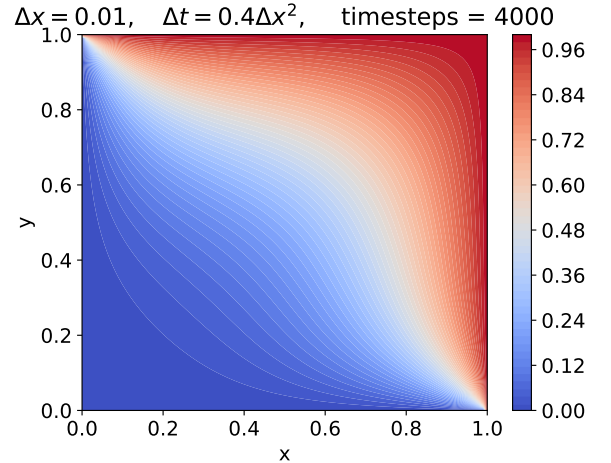

Figure 6. Same as figure 5, but advanced forward 4000 timesteps.

a more complex case, we plotted $u(x, y, t)$ without periodic boundary conditions and new boundaries in figures 5 and 6. The first figure shows the situation after 40 timesteps, where we clearly see the boundaries at $x = 1$ and $y = 1$, but not much diffusion outside these boundaries. At 4000 timestep in the second figure we see a system where the signal from the boundaries have diffused towards the centre of the grid. Looking at the point where $u = 0.5$ however, we see that the system still leans more towards $u = 0$ on average.
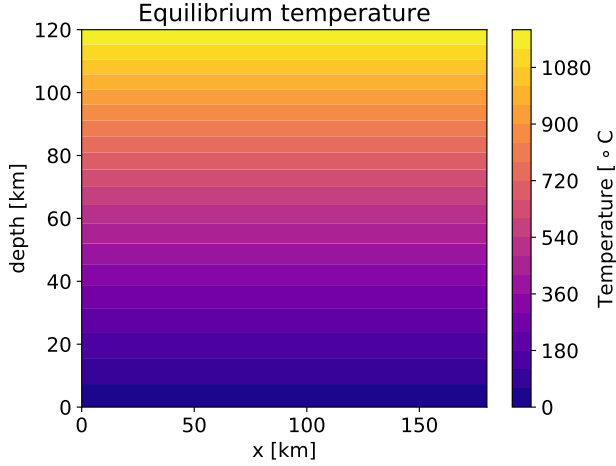
Figure 7. Temperature distribution of the litosphere after $\hat{t} = 0.2$ without any heat production caused by radioactive decay. The boundary conditions are $T(x, y = 0, t) = 0°C$ and $T(x, y = 0, t) = 1300°C$. The initial conditions are $T(x, y, t = 0) = 0°C$. The x-axis is periodic distance parallel to the surface, while the y-axis is depth below the surface, both in units of km. x lies in $[0, 180]$km while y lies in $[0, 120]$km.

C. Litosphere subject to radioactive enrichment

Applying the transformations described in II C, figure 7 shows the temperature after a non-dimensional time $\hat{t} = 0.2$ only applying the boundaries of temperature 0km and at 120km and with initial condition of $T = 0$ everywhere else. We see from the figure that the temperature has become linearly distributed between the boundary temperatures, hence we call this the equilibrium temperature.

Starting with the system in equilibrium, we modeled the three different cases of radioactive enrichment introduced in II C 1 Gyr forward in time, and plotted the resulting change ΔT from the equilibrium temperature. Case 1 was standard heat production, case 2 was an additional $0.5\mu W/m^3$ in the mantle, and case 3 was with this additional heat distributed evenly between three elements with certain halvlives. The resulting plots are shown in figures 8, 9 and 10 respectively.

For the standard case in figure 8 we see an additional temperature of up to $64°C$ near the crust after 1 Gyr. The additional temperature decreases towards the mantle and the surface. We also note that the system is essentially independent of the lateral distance x.

With additional radioactive enrichment from a proposed subduction zone, we see from figures 9 and 10 that the system is no longer independent of x. Now, the temperature near the crust peaks $8°C$ higher at $72°$. For the case where the radioactive heat continues at the same rate regardless of time in figure 9, we see that the temperature change between 40 and 80 km depth between the lower crust and the mantle is comparable to the change
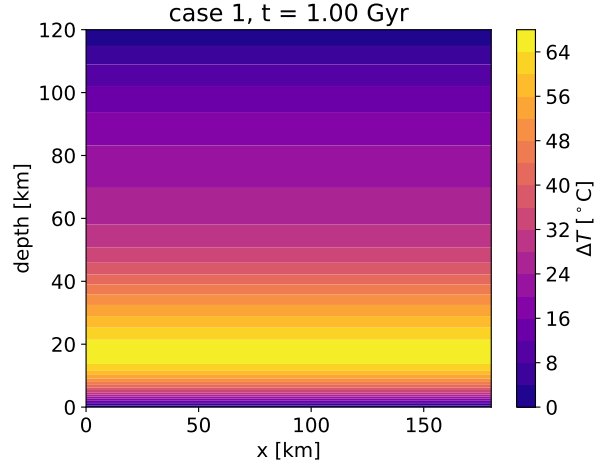

Figure 8. Case 1 system after 1 Gyr. Initial conditions given by the final state in figure 7. Dimensions of the box and boundary conditions are the same.
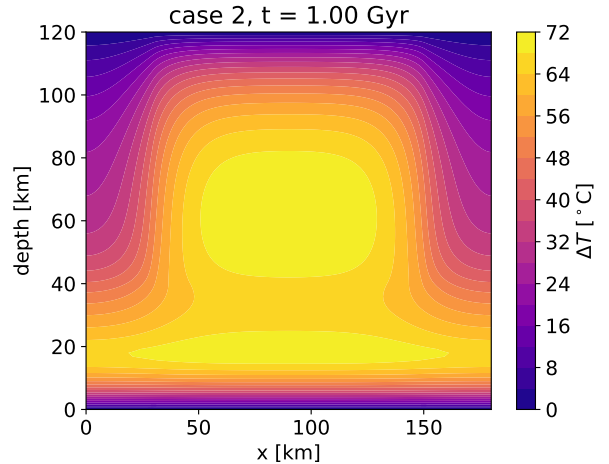

Figure 9. Shows the case 2 system after 1 Gyr. Initial conditions given by the final state in figure 7. Dimensions of the box and boundary conditions are the same.

near the upper crust. In figure 10, we see that it is comparable to the maximum temperature change in figure 8. We also note that the dependence on x happens in the form of a centered ball of heat in the centre of the 150 km wide area above the slab.

Figures 11 and 12 shows the case 2 and 3 figures evolved 20 times further in time until $t = 20$ Gyr, i.e. 19 billion years in the future (if the earth is still fine somehow). Here, we see similar situations between the two cases, both with a small centered peak in ΔT. For the permanent radioactive enrichment in figure 11 we see a high maximum temperature change of $\Delta T = 450°C$ 60 km below the surface in the upper mantle. In figure 12 with most radiation gone, the maximum $\Delta T = 270°C$ is centered about 50 km below the mantle.

Figure 10. Shows the case 3 system after 1 Gyr. Initial conditions given by the final state in figure 7. Dimensions of the box and boundary conditions are the same.
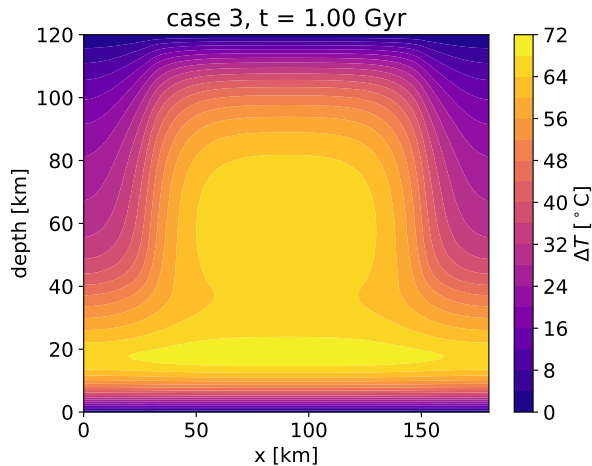

Figure 12. Shows the case 3 system after 20 Gyr. Initial conditions given by the final state in figure 7. Dimensions of the box and boundary conditions are the same.
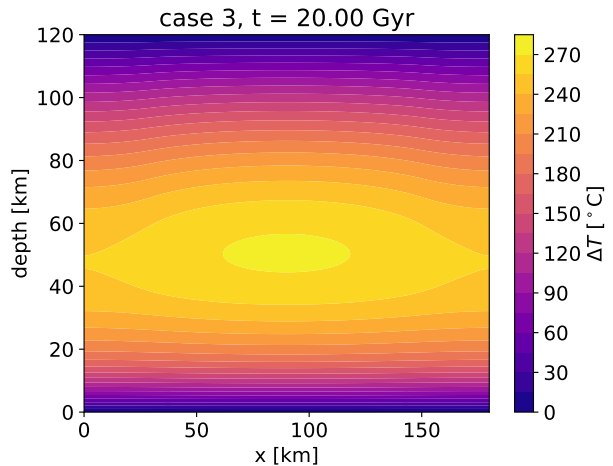

Figure 11. Shows the case 2 system after 20 Gyr. Initial conditions given by the final state in figure 7. Dimensions of the box and boundary conditions are the same.

IV. DISCUSSION

A. 1D-case

Starting with our results from the 1D case we see from figure 1 that even with only 9 discrete points between the boundaries and Δt close to the stability limit of $0.5\Delta x^2$ in the Euler forward method, all of the numerical schemes give results close to the analytical solution. This seems to indicate that at least in the 1D case, they are all valid choices for this system if we do not require very high accuracy.

If we want high accuracy, figure 2 is more telling for which of the methods we should choose. Here, we had analytically that the CN (Crank-Nicolson) method should have a truncation error $\propto \Delta x^2 \Delta t^2$, compared to the Euler methods at Δt. The figure indeed seems to indicate that CN gives more accurate results. Looking at the estimate at t_1 in particular, we also see some indication for why this is the case.

While the forward Euler method consistently overestimates $u(x,t)$, backward Euler consistently underestimates $u(x,t)$. This might be because the Euler methods are linear methods for approximating derivatives, while $u(x,t)$ is curved with some detail in second and higher derivatives. If the curve is consistently concave or convex, we would expect the Euler methods to consistently miss in the same 'direction', which might be what we see in this plot. As for why the CN method is better here, we recall that it essentially combines a step of the EF (forward Euler) method with a step of the EB (backward Euler method), thus making estimates towards the middle of a curve instead of missing underneath or above the curve. At t_1, this might be reflected by how the CN error lies both above and below the analytical solution
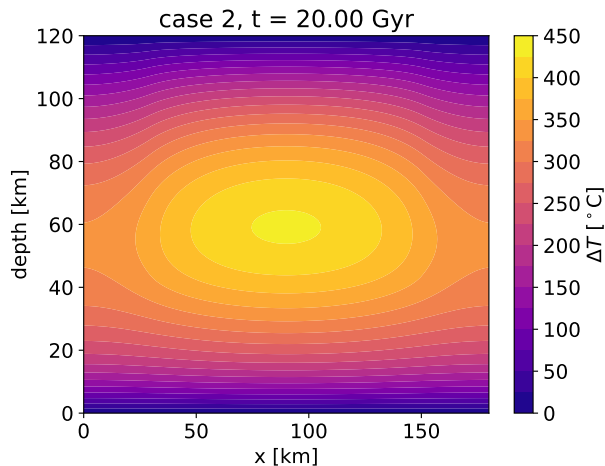
for different x. At t_2, the EF method is closer to the CN in terms of error, which might be because $u(x, t)$ is now starting to become linear.

In fact, it might seem that if we consider a system which is linear in equilibrium, the CN method is not necessarily better than the Euler methods. At least for the explicit EF method, we see from figure 4 that the mean absolute average error is in fact lower than for the CN method when we choose low enough values of Δt. However, if we wanted to integrate far forward in time, fewer time steps would be required at the minimal error of the CN method. Whether or not this compensates for the increased computational time of this implicit method could be interesting for further work.

Nevertheless, we see from figure 3 that when $u(x, t)$ is curved, the CN method generally works best. Although they all seem to reach a minimum error of about 10^{-3} for $\Delta x = 0.1$ and 10^{-5} for $\Delta x = 0.01$, the Euler methods quickly starts to increase proportional to Δt while the CN error remains constant. Although the increase of error according to Δx^2 is what we would expect from our analytical results of the local truncation error, the error increase with Δt is not what we would expect. If we consider the global accumulated error which is shown in the figures, we note that an increase in Δt will give a proportional increase in the total time steps, which gives a maximum accumulated error of $1/\Delta t$ times the local error. Here we had a local error $\propto \Delta t$ for the Euler methods and $\propto \Delta t^2$ for the CN method, which should give global errors of respectively $\propto$ constant and $\propto \Delta t$, where the opposite is what we see.

A possible reason for why we still see this result is that this maximum accumulated error assumes that all the local errors have the same sign so that they add up, but this won't necessarily be the case. If not, then it seems reasonable that the local error is representative for the global error as it appears for the Euler methods. As for why the CN method then does not increase with Δt^2, we start by noting that from both the figures 3 and 4, we see that towards high Δt it does in fact start to increase near this rate. As for why it remains constant at lower Δt, this could be because the truncation error is not what dominates here. This also explains why the Euler methods also seem to approach constant values for low enough Δt. They remain at a constant error for shorter time because their higher truncation error starts to dominate earlier.

One final thing to mention from figures 3 and 4 is that we see that at a multiplier of 0.5, which we found analytically to be the stability limit for the Euler forward method, this explicit method indeed seems to become unstable here.

Concluding the results from the 1D case, we have confirmed that the CN method is more accurate than the Euler methods when the truncation error dominates and the function that is being modeled does not have a near linear shape.

B. 2D case

Moving on to the 2D case then, we know that for the later physical modeling, we consider systems near equilibrium and with near linear distributions of temperature. For this reason, extending the Euler approach to one extra spatial dimension should not be unreasonable, and way simpler to implement. Predicting a stricter stability criterion with $\Delta t \leq 0.25\Delta x^2$ analytically, we still wanted to investigate exactly how the error depends on Δx and Δt in the 2D case.

From the global error in I, we found that it goes as $\epsilon_{global} \propto \Delta x$, recalling that $\Delta x = \Delta y$ in our case. For $\Delta t = 0.4\Delta x^2$ which is higher than the stability criterion, we indeed see that the solution is not stable. For lower Δt however, there appears to be no point in decreasing Δt further if a better global error is desired. This is consistent with what we expected to see in the 1D case, which according to what we discussed would mean that the errors for each step have similar signs here and get combined into an error proportional to the amount of timesteps.

This understanding is consistent with the local error seen in II which goes as $\epsilon_{local} \propto \Delta x \Delta t$. As for why the proportionality of Δx does not change, we note that the error is averaged over the absolute of all values in the grid, so it is still local with respect to x and y in this sense.

We note that the choice of $\Delta x = 0.025$ resulted in an global average error of 0.05 after $t = 0.2$. We therefore choose $\Delta x = 0.01$ for further analysis, which should give results within about 2% accuracy for similar time scales, and more accurate results for shorter time scales.

First plotting results for different boundaries in figures 5 and 6, we see that as time goes on, the system moves from the initial condition at $u(x, y, t = 0) = 0$ towards a more stable equilibrium. Intuitively, we would expect this equilibrium to yield a line of $y = 0.5$ between the top left and bottom right corner of these plots, which symmetrically separates the boundary values of $y = 0$ and $y = 1$. Looking at figure 6 this is close to happening. This indicates that the required time to reach equilibrium in this system is about $4000\Delta t = 4000 \cdot (0.4 \cdot 10^{-4}) = 0.16$.

Modeling the Litosphere

In the proposed equilibrium state in figure 7, we simulated for a dimensionless time of $t = 0.2$ which is a bit longer than this equilibrium timescale. This system is equivalent to the periodic case we studied for the general 2d equations, except for a small boundary at $\hat{y} = 0$ as

well. Here we had the analytical solution which should give a linear increase when the system has reached equilibrium, which we would also expect to be the case here along the y-axis. The results in figure 7 seems consistent with this, so we conclude that we have indeed reached the equilibrium state for the given boundary conditions.

Simulating further for the various total radioactive enrichment, we first consider the case 1 results in figure 8. Since Q has its largest value of $1.4\mu W/m^3$ between 0 and 20 km, it seems reasonable that this is where the temperature change is the largest. As for why it tends a bit more towards 20 km than 0 km, this is because of the forced boundary of $T = 8 * \circ C$ at the surface. We also note that between 60 and 80 km depth, we have a couple of wider lines, showing that lower crust and mantle heat production also have effects, albeit smaller.

Looking at the results attempting to model the subduction zone off the coast of Norway 1 billion years ago, we first look at figure 9 which does not take into account the half life of the heat producing radioactive elements. Here, we see that the temperature effect is comparable in size to the standard radioactive enrichment in case 1, and a large area in the upper mantle heats up significantly. We also note that we see the imposed 150 km width of the effects from the subducted slab, since we no longer have equal situations for all values of y. In fact, the highest ΔT appears to occur in about the central 100 km of this area, decreasing rapidly towards positive and negative directions of x. The decrease is lessened as we move nearer the surface because the default radioactive heating is assumed to be over all x.

Note that the temperature values outside the 150 km central area (between 15 and 165 km) are a bit higher than they should be because our periodic boundary conditions essentially implies that there's a neighbouring slab centered 180 km away. This could have been prevented if we increased the length along the x-axis, but since the contour curves appear rather flat we decided it sufficiently accurate.

Moving on to figure 10 including the realistic effects of radioactive decay, we have reached the most realistic model that we present in this report for the litosphere underneath today's Oslo. Here, we see that although a bit less, the heating of the lower mantle is still significant at around $60°C$. Looking at figure 7, we see that this corresponds to an increase in temperature of about 10% in the relevant depths. There is also the increase of about $8°C$ in the warmest parts of the crust, which is about 5% of the temperature without taking these effects into account. All in all, we conclude that the subduction zone

on the western coast about 1 billion years ago does indeed have a noticeable impact on the temperature of both the crust and the mantle today.

Skipping a bit further ahead in time to the year 19 billion 2020, we found stable circles in both the non-decaying and decaying element cases in figures 11 and 12. It seems that equilibrium has been reached at this point in time, where the more shallow equilibrium in the decaying case makes sense since the standard heat contribution of $1.4\mu W/m^3$ near the crust will dominate. Also note the very high ΔT at 450 and 270 degrees Celsius in case 2 and 3 respectively. With a constant heat production without any means of heat escape, it makes sense that the temperature will become much higher eventually. In this sense, one weakness of our model is that we indeed have no heat escape, which might be unrealistic compared to the real world. On the 1 Gyr timescale, however, it might be that such effects are neglibible in comparison.

V. CONCLUSION

With the goal of modeling the temperature distribution in the litosphere underneath Oslo, we have numerically solved the diffusion equation. We first considered a simple one-dimensional case to determine an appropriate scheme for advancing the system forward in time. Comparing to the analytical solution and seeing that the explicit forward Euler method gives reasonable results, we extended the diffusion equation to two dimensions. We then saw that the accuracy was good given a sufficiently low spatial step-size $\Delta x = \Delta y \leq 0.025$ and a time-step Δt that satisfied $\Delta t < 0.25\Delta x^2$.

Modeling a system with more complex boundary conditions, we estimated a time needed to reach equilibrium, which we used to model the equilibrium state of the litosphere with given boundary temperatures at the surface and lower mantle. We further studied three different cases of heat from radioactive enrichment, with the third one aimed at best representing the effects from the subduction zone off the western coast of Norway 1 billion years ago on the litosphere today. We found increases in temperature due to this subduction zone of about $5-10\%$ in the crust and lower mantle, concluding that such an event should indeed have effect on the litosphere today.

For future work, a more complex numerical scheme could be used for more accurate results.

[1] M. Hjorth-Jensen, "Computational physics," August 2015.

[2] J. Crank and P. Nicolson, "A practical method for numerical evaluation of solutions of partial differential equations of the heat-conduction type," *Mathematical Proceedings of the Cambridge Philosophical Society*, vol. 43, no. 1, p. 50–67, 1947.

VI.   APPENDIX A: THEORY

Analytical solution to 1D-case

Assuming solutions to $u(x,t)$ have the form $u(x,t) = F(x)G(t)$, we can insert into the partial differential equation (2) to get

$$GF'' = F\dot{G} \implies \frac{F''}{F} = \frac{\dot{G}}{G}.$$

For this to hold for all values of x and t, both sides of the equation must be constant values. Labeling this constant by $-\lambda^2$, this gives two ordinary differential equations

$$F'' = -\lambda^2 F, \quad \dot{G} = -\lambda^2 G.$$

Assuming $\lambda \neq 0$, these equations have general solutions

$$F(x) = A sin(\lambda x) + B cos(\lambda x), \quad G(t) = C e^{-\lambda^2 t}.$$

Looking at the particular case of $\lambda = 0$, we have $F''(x) = 0 \implies F(x) = Ax + B$ and $\dot{G}(t) = 0 \implies G(t) = C$. This solution is a straight line which is constant in time. With boundaries at $u(0,t) = 0$ and $u(1,t) = 1$, we must therefore have $u(x,t) = x$ as one of the solutions to the PDE. Since the PDE is linear, we further know that solutions $u(x,t)$ can be expressed as a sum of particular solutions, so we define $u(x,t) = x + F(x)G(t)$. Doing this is useful because the boundary values of $F(x)G(t)$ will now both be zero, where

By the boundary conditions, we then have

$$u(x = 0, t) = 0 + F(0)G(t) = 0 \implies F(0) = B = 0$$
$$u(x = 1, t) = 1 + F(1)G(t) = 1 \implies F(1) = A sin(\lambda) = 0$$
$$\implies \lambda_n = n\pi, \quad n \in \mathbb{N}.$$

Here, we have infinite solutions for different values of n, and the constant A is yet to be determined. For some n,

the solution is now on the form

$$u(x,t) = x + F(x)G(t) = x + A sin(n\pi x)C e^{-(n\pi)^2 t}.$$

We combine the undetermined constants A and C into the constant A_n, which will differ with the value of n. To evaluate this constant, we can finally impose the initial conditions. Note that although $u_n(x,t)$ solved the equation with boundary conditions, a single such solution is not enough to satisfy these initial conditions, as $u(x,0) = x + A_n sin(n\pi x)$ cannot be 0 everywhere. Instead, we can satisfy the initial conditions by constructing a solution $u(x,t)$ as a linear combination of infinite $u_n(x,t)$, going from $n = 1$ to $n = \infty$. We then require

$$u(x,0) = 0 = x + \sum_{n=1}^{\infty} A_n sin(n\pi x) \Rightarrow \sum_{n=1}^{\infty} A_n sin(n\pi x) = -x.$$

The coefficients A_n are now the Fourier coefficients for the function $-x$, so from theory on Fourier Series we then have that the A_n are given by

$$A_n = 2 \int_0^1 -x sin(n\pi x) dx = -2\left(\frac{sin(\pi n) - \pi n cos(\pi n)}{\pi^2 n^2}\right)$$
$$= \frac{2\pi n}{\pi^2 n^2} cos(\pi n) = \frac{2 \cdot (-1)^n}{\pi n}.$$

Thus, we have that the solution to the PDE formulated in (2) with our chosen boundary and initial conditions is given by

$$u(x,t) = x + \sum_{n=1}^{\infty} \frac{2 \cdot (-1)^n}{\pi n} sin(n\pi x) e^{-(n\pi)^2 t}. \quad (8)$$